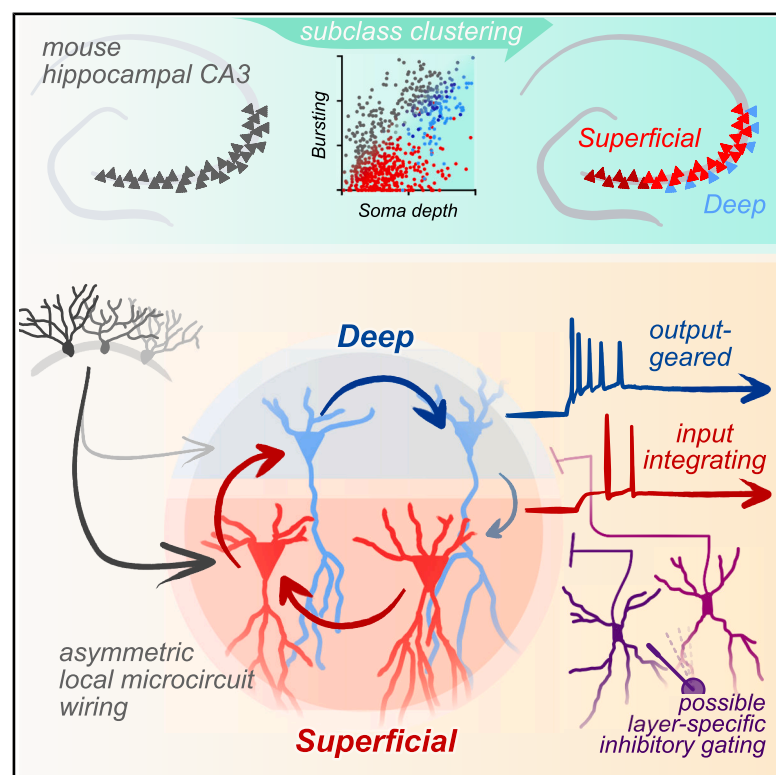# Cell-specific wiring routes information flow through hippocampal CA3

Graphical abstract

Authors

Jake F. Watson, Victor Vargas-Barroso, Peter Jonas

Correspondence

jake.watson@ist.ac.at (J.F.W.),
peter.jonas@ist.ac.at (P.J.)

In brief

The hippocampal CA3 recurrent network is important for memory storage. Watson et al. show that in mouse CA3, heterogeneous pyramidal neurons form subclasses with different somatic locations (deep and superficial), non-random recurrent wiring, and apparent subclass-specific inhibition. These properties complexify hippocampal activity flow, potentially increasing the circuit's computational power.

Highlights

- "Deep" and "superficial" CA3 pyramidal neurons can be morpho-functionally subclustered

- Subclass-specific synaptic connectivity splits CA3 into parallel local recurrent circuits

- Subtypes have distinct cellular input-output features but no synapse-specific properties

- Correlation of synaptic inputs suggests subclass-specific inhibitory innervation

CellPress

Article

Cell-specific wiring routes information flow through hippocampal CA3

Jake F. Watson,[1,*] Victor Vargas-Barroso,[1] and Peter Jonas[1,2,*]
[1]Institute of Science and Technology (ISTA), 3400 Klosterneuburg, Austria
[2]Lead contact
*Correspondence: jake.watson@ist.ac.at (J.F.W.), peter.jonas@ist.ac.at (P.J.)
https://doi.org/10.1016/j.celrep.2025.116080

SUMMARY

The hippocampus, critical for learning and memory, is dogmatically described as a trisynaptic circuit where dentate gyrus granule cells (GCs), CA3 pyramidal neurons (PNs), and CA1 PNs are serially connected. However, CA3 also forms an autoassociative network, and its PNs have diverse morphologies, intrinsic properties, and GC input levels. How PN subtypes compose this recurrent network is unknown. To determine the synaptic arrangement of identified CA3 PNs, we combine multicellular patch-clamp recording and post hoc morphological analysis in mouse hippocampal slices. PNs can be divided into distinct "superficial" and "deep" subclasses, the latter including previously reported "athorny" cells. Subclasses have distinct input-output transformations and asymmetric connectivity, which is more abundant from superficial to deep PNs, splitting CA3 locally into two parallel recurrent networks. Coincident spontaneous inhibition occurs frequently within but not between subclasses, implying subclass-specific inhibitory innervation. Our results suggest two separately controlled sublayers for parallel information processing in hippocampal CA3.

INTRODUCTION

The hippocampus plays a key role in learning and memory.[1] Patients in whom the hippocampus was bilaterally removed for therapeutic reasons are unable to acquire new memories.[2] Thus, neuronal activity flowing through the hippocampus is critical for information storage. However, the underlying circuit mechanisms remain elusive. Classically, the hippocampus is depicted as a trisynaptic circuit in which granule cells (GCs), CA3 pyramidal neurons (PNs), and CA1 PNs are serially connected.[3,4] However, both synaptic wiring and cellular properties are more complex than anticipated.

One level of complexity is added by synaptic connectivity, which is much more sophisticated than the simple trisynaptic circuit model. First, CA3 PNs not only connect to CA1 PNs along the trisynaptic pathway but also form recurrent synaptic connections with one another, establishing the largest autoassociative network in the brain.[5] These synapses are believed to be important for the storage of engrams and play a key role in higher-order computations, such as pattern completion.[6,7] Second, CA3 and CA1 PNs not only receive synaptic input along the trisynaptic loop but also direct projections from superficial and deep layers of the entorhinal cortex (EC).[8,9] Third, the presence of a distinct CA2 region adds further complexity to the circuit.[10] To understand how the flow of information through the hippocampus leads to the storage and retrieval of memories, it is necessary to precisely define the hippocampal connectivity map. Currently, such data are unavailable.

Another level of complexity is generated by principal neuron (PN) diversity.[11] In hippocampal CA1, superficial calbindin^{+} cells and deep calbindin^{−} neurons can be distinguished[12,13] and show different layer densities, genetics, and wiring,[14,15] resulting in specialized contributions to population coding.[16–20] In hippocampal CA3, the evidence for cell diversity is less compelling. Early studies provided evidence for subpopulations of "long-shaft" PNs, with less complex dendritic trees and fewer thorny excrescences,[21] and burst-firing PNs,[22] both with deeper somatic location. Recent work has suggested that CA3 PNs can be subdivided based on the presence or absence of mossy fiber input into "thorny" and "athorny" subpopulations.[23] However, in other studies, functionally identified PN subclusters showed less strict mossy fiber innervation rules,[24–26] while athorny PNs are yet to be observed in human CA3.[27] Whether these diverse properties represent distinct cell types or reflect continuous gradients[28,29] also remains uncertain. Finally, recent gene-expression studies identified several genetically distinct subtypes of CA3 pyramidal cells.[11,30,31] How genetic subtypes correspond to morphological subclasses is unknown, and whether these subtypes show distinct wiring within the recurrent network remains to be determined.

To address these questions, we combined multicellular patch-clamp-based circuit mapping with post hoc morphological analysis. This approach allowed us to determine the local synaptic connectivity of rigorously identified, physiologically and morphologically characterized CA3 pyramidal cells. We found that superficial and deep CA3 PNs segregated into distinct morpho-functional subclasses and showed non-random, asymmetric interconnectivity. These properties suggest a bifurcation of the transhippocampal information stream, initiating parallel signal processing in the core region of the hippocampal circuit.
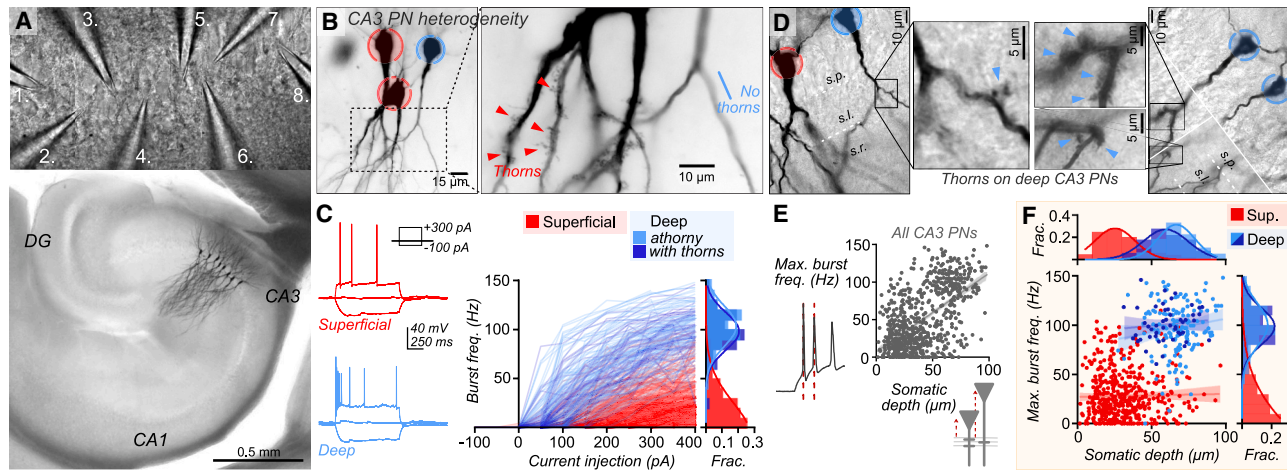
Figure 1. CA3 pyramidal neurons (PNs) form superficial and deep subclasses

(A) Infrared differential interference contrast (DIC) view of microelectrode pipettes (numbered) during multicellular recording (top) and DAB-stained hippocampal slice after octuple recording in CA3 (bottom). Scale bar: 0.5 mm.

(B) Light micrographs of CA3 PNs show cells with (red) or without (blue) thorny excrescences. Scale bar: 15 μm, inset: 10 μm.

(C) Analysis of action potential (AP) phenotypes evoked by long current pulses (representative traces, left; frequency-current curves, middle) showed distinct trajectories of initial burst frequency upon increasing current injection between PN classes (thorny/superficial and athorny/deep). A population of deep neurons with evident thorny excrescences (deep with thorns) had a similar firing profile to deep neurons without thorny excrescences (deep athorny). Burst frequency at 400 pA injection is also presented as a relative fraction histogram, fitted with Gaussian curves (right).

(D) Example micrographs of deep PNs displaying equivalent morphology to athorny neurons but with sparse thorny excrescences (arrowheads). s.p., *stratum pyramidale*; s.l., *stratum lucidum*; s.r., *stratum radiatum*. Layer boundaries are denoted by dashed white lines. A composite *z*-plane image (right) is presented for visualization of multiple structures. The boundaries between images are depicted with continuous white lines. Scale bar: 10 μm, insets: 5 μm.

(E) Scatterplots of maximal burst frequency upon current injection and somatic depth (distance from *stratum lucidum*) for all CA3 PNs show distinct clusters and overall positive correlation (gray line, linear regression: slope = 1.04 Hz μm^{-1}, R^2 = 0.33, $p < 0.0001$).

(F) Morphological assignment of PNs shows almost complete separation of PNs into the two clusters. Morphologically athorny-like neurons with evident thorns (dark blue) populate the deep cluster, demonstrating that athorny neurons form part of a larger subclass of deep CA3 PNs. No significant correlation between maximal burst frequency and somatic depth was observed within clusters, confirming that PNs form discrete subclasses rather than one heterogeneous gradient (colored lines, linear regressions; superficial: slope = 0.03 Hz μm^{-1}, R^2 = 0.00, and $p = 0.63$; deep [athorny]: slope = 0.28 Hz μm^{-1}, R^2 = 0.02, and $p = 0.10$; deep [with thorns]: slope = 0.14 Hz μm^{-1}, R^2 = 0.01, and $p = 0.46$). Relative fractional histograms for each axis are depicted with Gaussian fits.

See also Figures S1 and S2.

Preliminary accounts of the work were previously published in abstract form (Watson et al., 2022; Soc. Neurosci. Abstr. 019.06).

RESULTS

Different CA3 PN subclasses coexist on the deep-superficial axis

To determine the connectivity properties in the CA3 recurrent circuitry, we performed multicellular patch-clamp-based circuit mapping in acute slices of the mouse hippocampus. In total, we recorded 928 CA3 PNs. Coupled with post hoc visualization using 3,3′-diaminobenzidine (DAB) as the chromogen, this approach allowed a full functional and morphological analysis of cellular heterogeneity at the microcircuit level (Figure 1A). A hallmark feature of CA3 PNs is the presence of complex "thorny excrescences" on primary dendrites, the postsynaptic sites of GC input,[32] yet a subpopulation of neurons lacking these structures has been reported (athorny neurons).[23] Visualization of our recorded cells confirmed multiple examples of such neurons (Figure 1B), which, as characterized,[23,33] also displayed "burst-like" activity patterns on current injection and had a deep somatic location in *stratum pyramidale* (Figure 1C). These neu-

rons showed a characteristic dendritic arborization pattern, where the primary dendrite crossed *stratum pyramidale* before branching.[23] In addition to these cells, however, we encountered a substantial population of neurons with long dendritic shafts, deep somatic location, and burst-firing profiles similar to athorny neurons but also with sparse thorny excrescences (Figure 1D).

We therefore sought to determine if putative athorny neurons were indeed a discrete subclass of PNs as previously proposed or if they represent the end of a heterogeneous gradient of neurons with differing mossy fiber input and firing patterns. To address this question, we plotted maximal burst frequency upon current injection against somatic depth (distance from *stratum lucidum*; Figure 1E). Only cells with sufficient recording and morphological quality were included in the analysis (see STAR Methods). Among all PNs, we observed a positive correlation between burst frequency and somatic depth; however, neurons were clustered into two clearly visible populations (Figure 1E). Mapping morphological identity onto these clusters showed that classical CA3 PNs mapped on the first cluster, whereas the previously described athorny cells[23] mapped on the second cluster (Figure 1F). The cells with sparse thorny excrescences also mapped onto the second cluster, co-clustering with athorny neurons. Thus, while CA3 PNs can be dissected into discrete

subclasses, "lack of thorny excrescences" is not a defining criterion. These conclusions are consistent not only with the original reports of CA3 cell heterogeneity[21,22] but also with recent studies showing that bursting CA3 PNs frequently have thorny excrescences in both mouse[26] and rat[25,34] CA3. In conclusion, while clear CA3 PN subclasses exist, these cell types can be better distinguished on the basis of burst firing and somatic location than the presence or absence of thorns. Therefore, we henceforth use the terminology "deep" and "superficial" to refer to the two CA3 PN subpopulations.

To further test the hypothesis that deep and superficial neurons represent distinct subclasses, we plotted linear regressions within morphologically identified clusters. If neurons were a continuous gradient, we would expect the linear relationship observed across all neurons to be maintained within subclusters. However, this was not the case. Positive correlation between burst frequency and somatic depth was abolished within subclasses (Figure 1F). Therefore, CA3 PNs can be separated into distinct subclasses based on firing properties and somatic location. Linear discriminant analysis (LDA) could reliably segregate subclasses, with 94% agreement to morphological classification alone. This served as a basis to assign all recorded neurons to either deep or superficial identity (Figures S1A–S1D; see STAR Methods for complete description), resulting in 531 putative superficial and 233 deep PNs. A minor subset of neurons had morphology substantially deviating from their assigned cluster and were excluded from further analysis (two putative superficial thorn-lacking neurons and three extensively thorny, deep bursting neurons with multiple primary apical dendrites; Figure S1E). Determining whether these neurons reflect within-subclass variability or represent further minor neuronal subclasses will require future investigation. It is important to note that electrophysiological recordings are not an unbiased means to quantify the exact proportion of cell types. As we increasingly targeted deep PNs in the course of our study, our dataset will overrepresent the proportion of this subclass. We estimate that the true proportion will be 10%–20%, consistent with the prediction of Hunt et al.[23]

Our dataset was recorded from mid to ventral CA3 of relatively young animals (postnatal day [P]20–30). We therefore sought to confirm that the athorny and sparsely thorny nature of deep PNs was not due to ongoing developmental processes. Performing recordings from CA3 PNs in 6- to 7-week-old animals, we observed a similar distribution of morpho-functional properties. Deep PNs could be classified using the same parameters as in younger animals and contained neurons with both athorny and sparsely thorny phenotypes (Figures S2A and S2B). We also asked whether deep PNs could be observed in dorsal CA3. As *stratum pyramidale* is more condensed in dorsal than ventral CA3, the same linear classification could not be applied to dorsal CA3 PNs. Nevertheless, we observed a subpopulation of burst-firing PNs with somatic location in the deeper half of *stratum pyramidale* (Figures S2D and S2E). These neurons had similar morphological characteristics, including sparse thorny excrescences, to deep PNs in ventral CA3. These results corroborate that deep and superficial PN subclasses are a feature of CA3 along the dorsoventral axis and across a wide developmental time range.

Differential synaptic connectivity of deep and superficial CA3 PNs

Next, we analyzed the local synaptic connectivity between PNs in the CA3 recurrent collateral network from our original dataset. We focused on source and target cell-specific differences in synaptic connectivity (Figures 2A–2C). After PN subclassification, we were able to test 3,114 possible connections and observed 85 functional monosynaptic connections. Due to slicing, this is likely an underestimate of synaptic connectivity in the intact brain, which we have previously estimated to be approximately 1.7-fold higher than that recorded in slices without further corrections.[27] Connectivity was similar between sexes or hemispheres (Figure S3A); therefore, all data were pooled.

Surprisingly, we discovered highly asymmetric wiring rules (Figure 2D): while superficial CA3 cells provided input to both PN subclasses (to superficial: 58/1,592 and to deep: 17/561 identified connections), deep cells showed prominent connectivity to other deep PNs (9/400 connections), yet connectivity from deep to superficial CA3 PNs was an order of magnitude lower (1/561 connections). Our results suggest that the CA3 PN recurrent network is not a simple random recurrent network but that subclass heterogeneity generates more complex activity flow. Superficial CA3 PNs appear to form the "textbook-style" CA3 recurrent circuit, with deep CA3 PNs receiving the output of this network and forming a separate recurrent network that sends little projection back to superficial CA3, at least at the local level.

CA3 is thought to form a broad recurrent network across the hippocampal structure. In line with this, we observed no bias for directional connectivity on the proximal-distal axis, with connections between neurons occurring both in the direction of the dentate gyrus (DG) and in the direction of CA2/1 (Figures 2E and S3B). No intersomatic distance dependence of connectivity was observed either, consistent with other reports in CA3 of rats, mice, and humans[6,27,35] (Figures 2E and S3C). We did, however, observe a bias for connectivity toward deeper neurons (Figure 2E), which is predominantly generated by the asymmetric connectivity between PN subclasses but is also observed trendwise within individual subclass datasets (Figure S3D). Previous work demonstrated changes in the properties of CA3 PNs on the transverse (proximal-to-distal) axis.[28,29] We could confirm the tendency for higher firing in proximal CA3 from our dataset (Figures S3E and S3F). This region also appeared to contain the fewest recorded deep CA3 PNs, as previously proposed for athorny cells[23] (Figure S3G). The low abundance of deep PNs and higher firing properties of superficial PNs correlate with the presence of the infrapyramidal blade of the mossy fiber tract in this CA3 subregion, which may therefore functionally and anatomically act as a distinct unit. Calculation of connectivity on the proximal-distal axis also showed an apparent bias in the targeting of superficial PN axons from other superficial neurons in proximal CA3 to more deep PNs in distal CA3 (Figure 2F). More extensive analysis is required to confirm these trends.

In summary, we demonstrate subtype-specific differences in connectivity between superficial and deep CA3 PNs. The hippocampal CA3 region is not simply an additional station in the trisynaptic circuit but rather forms a two-layered recurrent network in which incoming information may be processed differently in the two layers.
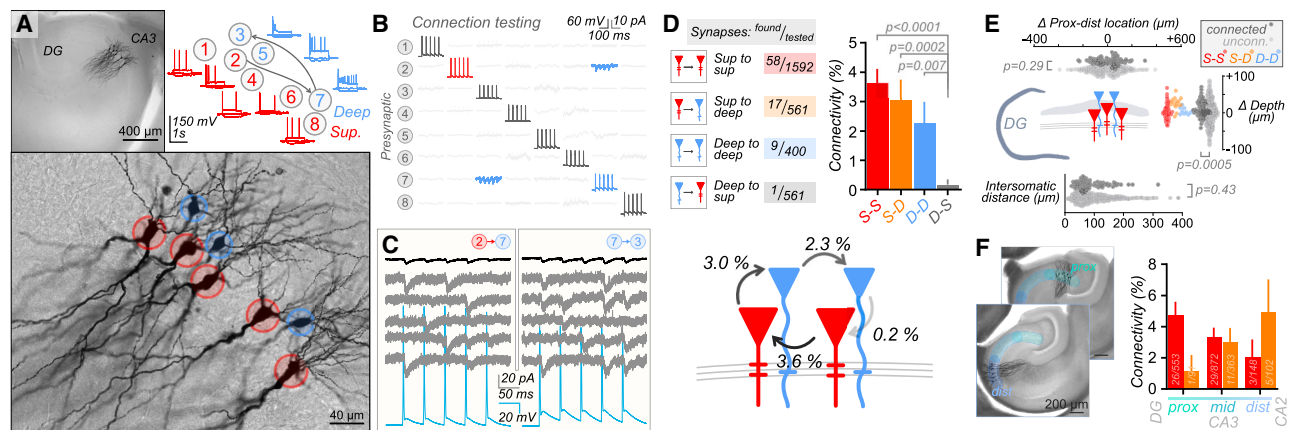
Figure 2. Deep and superficial subclasses have asymmetric connectivity in the CA3 recurrent network

(A) Example octuple recording from CA3, including both deep (blue) and superficial (red) subclasses. Micrographs at low (top) and high (bottom) magnification depict neuronal morphologies, with the cell identity labeled (color). The identified synaptic connectivity (arrows) is schematically depicted, alongside firing profiles for each neuron (−100, 0, and +400 pA injection traces displayed). Scale bars: 400 μm (low magnification) and 40 μm (high magnification).

(B) Voltage-clamp connectivity testing matrix for cells recorded in (A), with monosynaptic connections presented as bold and traces involved in connections colored by cell type. Each row presents an individual recording, with action potential generation in one cell (presynaptic, current-clamp), and voltage-clamp responses of all other cells.

(C) Synaptic traces from (B). Presynaptic APs (cyan) are followed at short latency by postsynaptic excitatory postsynaptic currents (EPSCs). Both postsynaptic individual traces (gray) and average response (black) are presented.

(D) Pooled connectivity measures from all recordings demonstrate asymmetric connectivity in the CA3 recurrent network. Connections from superficial PNs to both superficial and deep PNs are evident, yet deep PNs connect almost exclusively with other deep PNs. Error bars present SD estimated from a binomial distribution. Connectivity (%), measured ± SD, S-S: 3.64% ± 0.47%, S-D: 3.03% ± 0.72%, D-D: 2.25% ± 0.74%, and D-S: 0.18% ± 0.18%; Fisher's exact test, $p < 0.0001$; p values of pairwise comparisons after Benjamini Hochberg correction are labeled.

(E) No bias for directional connectivity on the proximal-distal axis was observed (top; + values denote postsynaptic soma more distal [toward CA2/1] than presynaptic soma; unconnected, −0.1 ± 2.1 μm, $n = 2,910$; connected, 12.3 ± 11.4 μm, $n = 81$, Mann-Whitney test, $p = 0.29$). In addition, no intersomatic distance dependence to connectivity was observed (all PN subclass intersomatic distances, bottom: unconnected, 97.7 ± 1.1 μm, $n = 2,936$; connected, 92.1 ± 5.9 μm, $n = 83$; Mann-Whitney test, $p = 0.43$). However, overall CA3 PN connectivity was biased for connectivity toward deeper PNs (+ values denote deeper postsynaptic soma; all PN subclasses, right: unconnected, −0.3 ± 0.6 μm, $n = 2,996$; connected, 10.5 ± 2.4 μm, $n = 85$, Mann-Whitney test, $p = 0.0005$), likely in part due to asymmetric connectivity. Individual subclass distances are also plotted (color).

(F) Micrographs of example recordings from proximal (top) or distal (bottom) CA3. Breakdown of connectivity into proximal, mid, or distal CA3 for S-S and S-D connections (connectivity [%], measured ± SD; proximal, S-S: 4.7% ± 0.9% and S-D: 1.1% ± 1.1%; mid, S-S: 3.3% ± 0.6% and S-D: 3.0% ± 0.9%; and distal, S-S: 2.0% ± 1.2% and S-D: 4.9% ± 2.1%; Fisher's exact test, $p = 0.37$). Scale bar: 200 μm.
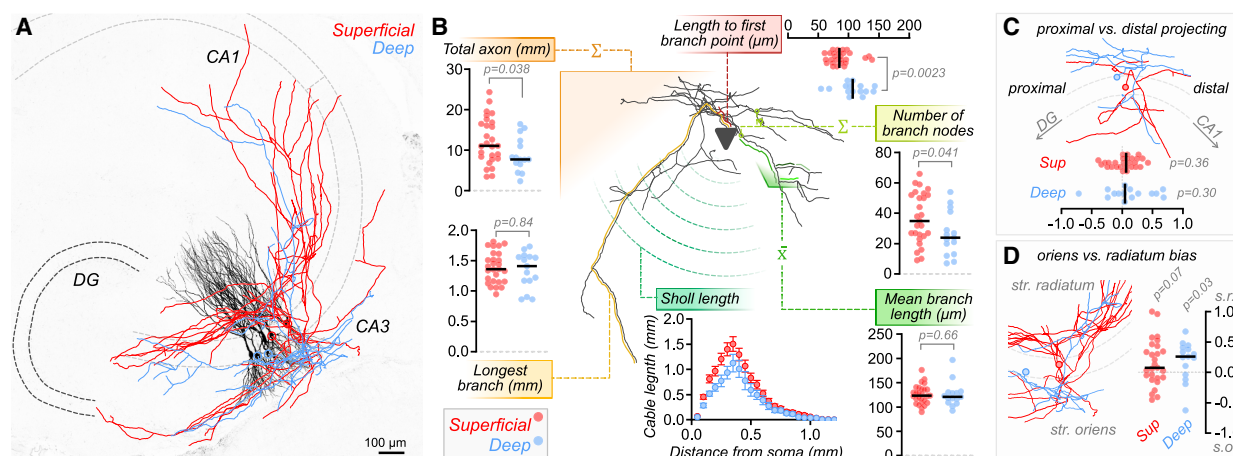
See also Figures S3 and S4.

Similar axonal arborization and unitary synaptic properties

To better understand the differences in local connectivity, we reconstructed the axonal arborization of deep and superficial PNs from a subset of fluorescently visualized, recorded neurons (Figure 3A). Axons of both subtypes showed extensive collateralization within the slice, albeit with greater axon length and a higher number of branch points for superficial than deep PNs (Figure 3B). Despite this effect, the broad axon pattern was highly similar between subtypes, with examples of both axons entering *stratum radiatum* of CA1 (Figure 3A), and similar projections in both the proximal and distal directions (Figure 3C). We observed a subtle bias of deep PNs to collateralize in *stratum radiatum* over *stratum oriens* (Figure 3D) and a small but robust difference in the location of the first branchpoint, which could potentially be used as an additional morphological diagnostic in future studies (Figure 3B). Together, these data do not suggest major differences in the local targets of deep and superficial PNs in CA3 and CA1; however, reduced collateralization of deep PNs likely results in fewer local postsynaptic cells.

We next studied the synaptic properties of unitary connections between CA3 PNs in the recurrent system. Excitatory postsynaptic current (EPSC) recordings displayed no subclass-dependent differences in potency, success rate, or latency of connections between CA3 PNs (Figure 4A). Synaptic kinetics were also similar across subclasses (Figure 4B). During 20 Hz trains, we observed subtly depressing average responses, which were driven more by a decrease in success rate than a change in potency (Figure 4C). Again, these properties appeared similar across PN subtypes. Taking these results together, it appears that while CA3 recurrent synapses have diverse and heterogeneous properties, these synapses are used similarly by PN subclasses.

When analyzing synaptic properties further, we observed a striking relationship between EPSC potency and success rate, following an exponential function (Figure 4D). Weaker synapses with lower synaptic potency not only produced a smaller synaptic current but were also the most unreliable. Conversely, more reliable synapses were exponentially more potent, producing an ~80-fold disparity in the overall transmission

Figure 3. Similar axon collateralization between PN subtypes

(A) Example image of recorded CA3 PNs (maximum intensity projection from fluorescence image stack) overlaid with reconstructed axons of two deep (blue) and two superficial (red) PNs. Both subtypes show collateralization in *stratum oriens* and *stratum radiatum*, both proximally and distally, and enter the CA1 subfield. Scale bar: 100 μm.

(B) More reduced axon collateralization was observed for deep than for superficial PNs, reflected in a reduced total axon length per cell (superficial, 12.3 ± 1.1 mm, $n = 27$; deep, 8.9 ± 1.1 mm, $n = 15$; Mann-Whitney test, $p = 0.038$), lower Sholl length analysis (50 μm bins), and less branch nodes per tree (superficial, 36.9 ± 3.2, $n = 27$; deep, 26.4 ± 3.7, $n = 15$; Mann-Whitney test, $p = 0.041$). The longest branch (soma to tip) and the mean distance between branch nodes were no different between subtypes (longest branch: superficial, 1.39 ± 0.05 mm, $n = 27$; deep, 1.34 ± 0.08 mm, $n = 15$; Mann-Whitney test, $p = 0.84$; mean branch length: superficial, 125.6 ± 6.5 μm, $n = 27$; deep, 125.7 ± 6.5 μm, $n = 15$; Mann-Whitney test, $p = 0.66$). The distance from soma to the first branchpoint was subtly increased for deep PNs (superficial, 87.3 ± 3.8 μm, $n = 27$; deep, 107.2 ± 6.2 μm, $n = 15$; Mann-Whitney test, $p = 0.0023$).

(C) No bias for collaterals projecting toward either proximal or distal CA3 was observed for either PN subtypes (bias index median: superficial, 0.07, $n = 27$; deep, 0.05, $n = 15$; one-sample Wilcoxon tests comparing median to "0.00": superficial, $p = 0.36$; deep, $p = 0.30$).

(D) However, a significantly greater proportion of deep PN collaterals were in *stratum radiatum* over *stratum oriens* (bias index median: superficial, 0.08, $n = 27$; deep, 0.26, $n = 15$; one-sample Wilcoxon tests comparing median to 0.00: superficial, $p = 0.07$; deep, $p = 0.03$). Indices are calculated as the difference between axon lengths in each condition (strata or direction) divided by total axon length, where 1 or −1 indicates complete bias.

strength between the weakest and strongest synapses. This relationship is consistent with a substantial variability in release probability or number of functional release sites across CA3-CA3 synapses, with multiquantal release likely to be occurring at strong synapses. This dataset of synaptic properties across the CA3 recurrent circuit may reflect the result of previous synaptic plasticity and engram storage. Therefore, there appears to be a significant presynaptic component of long-term storage at this connection, which works in tandem with postsynaptic mechanisms. Whether potential multiquantal release is occurring at single or multiple spine-bouton contacts will require high-resolution imaging of recurrent synapses.

We next examined excitatory postsynaptic potential (EPSP) properties. As previously observed in multiple species,[6,27,35,36] CA3-CA3 synapses were weak, with mean unitary depolarizations across all subclasses of just 0.94 ± 0.10 mV (EPSP potency; Figure 4E). Therefore, substantial synaptic integration will be required for spike generation by recurrent activity and associational network function. We observed no difference in EPSP potency between connection subtypes (Figure 4E), nor in temporal summation (Figure 4F); however, comparing the ratio of EPSP and EPSC peak amplitudes at the same synapse revealed a higher EPSP output for CA3 synapses onto deep PNs than superficial PNs (Figure 4G). To probe the mechanisms underlying this difference, we measured the input resistance of the postsynaptic superficial and deep neurons. Consistent with previous data,

input resistance was significantly higher in deep than in superficial neurons[23,26,33] (Figure 4H; 240 ± 3 vs. 261 ± 4 MΩ, $p < 0.0001$). This membrane property also likely contributes to the lower rheobase current observed for deep PNs (Figure 4H), which, together with burst firing, exemplifies the enhanced output properties of deep PNs. These differences between deep and superficial PNs were maintained in recordings from 6- to 7-week-old mice (Figure S2C). Overall, we observe no synapse-specific differences between CA3 subclasses, suggesting that CA3 recurrent synapses form a uniform population. How these synapses are used in circuit computations will be determined by the cell subclass they belong to, both through cell-specific input/output properties and the asymmetric wiring that we uncovered.

Further subclassification of non-bursting PNs into weak and strongly adapting cells has been performed previously.[26,37] We observed such a tendency within the superficial subclass of our dataset (Figure S4A). However, we found little spatial, functional, or connective differences between these cells (Figures S4B–S4D). Therefore, the significance of these differences for CA3 function remains to be clarified.

Correlated spontaneous activity suggests differential inhibitory innervation of CA3 PN subclasses

Our recordings allow analysis of not only evoked synaptic transmission between cells but also spontaneous input from unrecorded cells elsewhere in the slice, giving a measure of the input
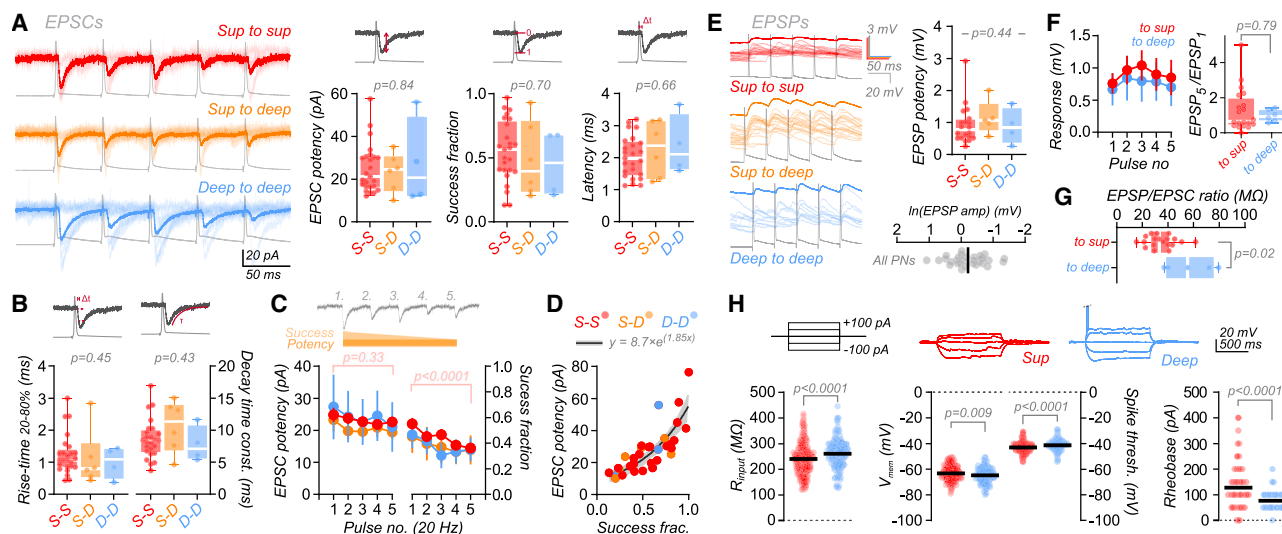
Figure 4. Recurrent synaptic properties are independent of CA3 PN subclass

(A) EPSCs of recurrent synapses between recorded CA3 PNs. Synaptic currents show no subclass-specific properties, with similar potencies (S-S: 24.9 ± 2.2 pA, n = 25; S-D: 23.3 ± 3.7 pA, n = 6; D-D: 27.3 ± 10.2 pA, n = 4. Kruskal-Wallis test, p = 0.84), success fraction (S-S: 0.55 ± 0.05, n = 25; S-D: 0.49 ± 0.12, n = 6; D-D: 0.45 ± 0.13, n = 4; Kruskal-Wallis test, p = 0.70), and latencies (S-S: 2.03 ± 0.13 ms, n = 25; S-D: 2.28 ± 0.35 ms, n = 6; D-D: 2.37 ± 0.47 ms, n = 4; Kruskal-Wallis test, p = 0.66).

(B) EPSC kinetics are also similar between subclasses (rise time [20%–80%], S-S: 1.24 ± 0.12 ms, n = 25; S-D: 1.10 ± 0.36; D-D: 1.00 ± 0.24, n = 4; Kruskal-Wallis test, p = 0.45; decay time constant, S-S: 8.6 ± 0.6 ms, n = 25; S-D: 10.6 ± 1.6 ms, n = 6; D-D: 7.8 ± 1.4 ms, n = 4; Kruskal-Wallis test, p = 0.43).

(C) Responses across 20-Hz train stimulation appear to be produced by events with similar potency (left) and a decreasing fraction of successes (right) (EPSC potency, two-way ANOVA with Tukey's multiple comparison tests: S-S pulse 1 vs. 5, p = 0.33; success fraction, S-S pulse 1 vs. 5, p < 0.0001).

(D) The relationship between synaptic potency and success fraction is independent of PN subclass but shows a striking exponential relationship (exponential fit of all data points, y = c exp(kx), R^2 = 0.65; fit and 95% confidence intervals are plotted as line and shading, respectively).

(E) EPSP amplitudes show no significant difference between PN subclasses (S-S: 0.92 ± 0.13 mV, n = 20; S-D: 1.15 ± 0.24 mV, n = 5; and D-D: 0.88 ± 0.28 mV, n = 4; Kruskal-Wallis test, p = 0.44). Overall, EPSPs follow a log-normal distribution, as demonstrated by plotting the natural log of amplitudes (lower; line at mean [−0.22 mV]; Shapiro-Wilk normality test, W = 0.98, p = 0.90).

(F) EPSP response during 20-Hz train stimulation shows similar temporal summation onto superficial (sup) and deep PNs ($EPSP_5/EPSP_1$ ratio: to superficial, 1.3 ± 0.3, n = 20; to deep, 1.0 ± 0.1, n = 6; Mann-Whitney test, p = 0.79).

(G) The EPSP-to-EPSC ratio of CA3 synapses onto deep PNs is greater than that onto sup PNs (CA3 PN synapses onto sup: 34.7 ± 2.6 MΩ, n = 19; onto deep PNs, 56.9 ± 8.4 MΩ, n = 5; Mann-Whitney test, p = 0.02).

(H) Intrinsic properties may explain this effect, with a higher input resistance at deep than at sup PNs (example traces have spikes truncated for presentation [dashed line]; plots have line at mean; R_{input}: sup PNs (red), 239.9 ± 3.2 MΩ, n = 354; deep (blue), 260.7 ± 4.5 MΩ, n = 171; Mann-Whitney test, p < 0.0001). Resting membrane potential is subtly lower in deep PNs (line at mean, sup: −63.2 ± 0.3 mV, n = 354; deep: −64.7 ± 0.47 mV, n = 171; Welch's t test, p = 0.009), and spike threshold is subtly higher (line at mean, sup: −42.6 ± 0.2 mV, n = 354; deep: −41.0 ± 0.3 mV, n = 164; Mann-Whitney test, p < 0.0001). The lower rheobase (current required for firing) in deep PNs is also a likely consequence of membrane properties (line at mean, sup: 127.7 ± 4.1 pA, n = 354; deep: 77.2 ± 2.6 pA, n = 171; Mann-Whitney test, p < 0.0001), making this CA3 PN subclass more sensitive to input currents.

levels to recorded cells. In our recording configuration, the chloride gradient generates inward currents for both glutamate- and GABA-mediated events, and therefore, spontaneous PSCs (sPSCs) represent a mixture of excitatory and inhibitory input. The frequency of sPSCs was significantly higher on superficial than deep PNs (5.4 ± 0.5 vs. 3.0 ± 0.4 Hz; Figure 5A). GABAzine application (10 μM) blocked a similar frequency of events between subclasses (superficial: 2.2 Hz, deep: 2.0 Hz), leaving a substantially lower frequency of excitatory events (sEPSCs) on deep than on superficial PNs (superficial: 3.2 ± 0.5 Hz, deep: 0.9 ± 0.2 Hz; Figure 5A). Recording noise was no different between subclasses, confirming that observations were not caused by differential event detection (Figure S5A). These data suggest that while inhibitory input levels are similar between PN subclasses, deep PNs receive substantially lower levels of spontaneous excitatory input or receive weaker input that falls below the level of recording noise. This is consistent

with the more limited dendritic branching of deep PNs identified in early reports of CA3 heterogeneity.[21] Therefore, the overall input-output balance between CA3 PN subclasses appears shifted, whereby superficial PNs receive and integrate greater levels of input, while deep PNs respond more strongly when receiving excitation.

Through recording multiple cells simultaneously, we observed instances where sPSCs occurred synchronously on two different cells. To determine whether this observation occurred by coincidence or through biological circuit mechanisms, we detected sPSCs and computed matrices of interevent intervals (IEIs) between all events on all recorded pairs of cells (Figure 5B; see also Rieubland et al.[38]). Plotting event crosscorrelograms with fine, 1 ms time bins showed striking peaks at Δt = 0 for a subpopulation of cell pairs. This indicated that a proportion of exquisitely synchronous inputs occurred significantly above the random level. As these events occurred primarily at two, but not more,
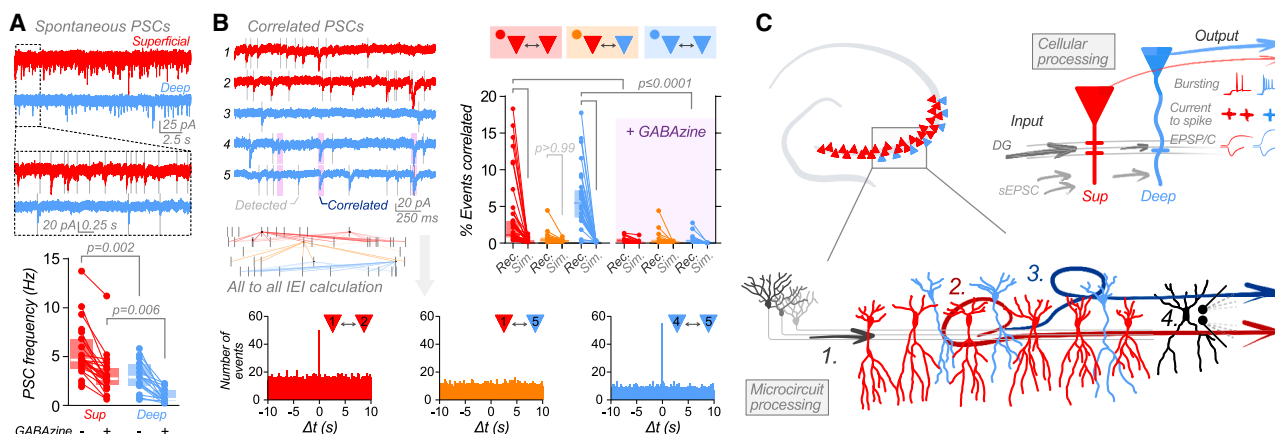
Figure 5. sPSC timing suggests subclass-specific inhibitory inputs

(A) sPSC frequency is higher on superficial (sup) than on deep PNs, suggesting more abundant or stronger synaptic input (sup: 5.37 ± 0.52 Hz, $n = 26$; deep: 2.96 ± 0.39 Hz, $n = 16$; Kruskal-Wallis test, $p < 0.0001$). Bath application of 10 µM GABAzine blocked a similar frequency of events from both subclasses (sup: 2.2 Hz, deep: 2.0 Hz blocked), meaning far less sEPSCs are recorded on deep PNs (sup: 3.20 ± 0.48 Hz, $n = 21$; deep: 0.94 ± 0.17 Hz, $n = 16$; Kruskal-Wallis test, $p < 0.0001$).

(B) Detected sPSCs (gray vertical bars) frequently displayed synchronous occurrences on different cells during multicellular recordings (pink highlights). Calculation of all interevent intervals (IEIs) between event times of different cells allows plotting of sPSC event correlation between cells (bottom). Histograms of IEIs (1 ms bin width) show sharp peaks specifically at $\Delta t = 0$ s, demonstrating strictly coincident events between cell pairs. Peaks are observed between sup cells (cells 1 vs. 2, red) and between deep cells (cells 4 vs. 5, blue) but not across classes (cells 1 vs. 5, orange). Quantification of the percentage of all events that are coincident between cell pairs (recorded [Rec.] < 0.5 ms IEI for inclusion) shows significant correlation above simulated (Sim.) random levels for within-cell-class but not between-cell-class comparisons (sup-sup [red], Rec.: 3.38% ± 0.69%, Sim.: 0.24% ± 0.05%, $n = 44$ pairs; sup-deep [orange], Rec.: 0.62% ± 0.15%, Sim.: 0.30% ± 0.04%, $n = 30$ pairs; deep-deep [blue], Rec.: 5.92% ± 0.69%, Sim.: 0.09% ± 0.02%, $n = 34$ pairs; Kruskal-Wallis test, $p < 0.0001$). Bath application of GABAzine (purple) substantially reduces the percentage correlation (sup-sup, Rec.: 0.39% ± 0.07%, Sim.: 0.10% ± 0.04%, $n = 34$ pairs; sup-deep, Rec.: 0.46% ± 0.16%, Sim.: 0.13% ± 0.03%, $n = 30$ pairs; deep-deep, Rec.: 0.43% ± 0.10%, Sim.: 0.00% ± 0.00%, $n = 32$ pairs; Kruskal-Wallis test, $p < 0.0001$), suggesting inhibitory inputs as a source. Data are from 12 multicellular recordings.

(C) Hippocampal CA3 contains distinct PN subclasses in two layers (deep [blue] and sup [red], top left). Intrinsic neuronal properties display different input-output balance, with deep neurons receiving less input but tuned to provide more output when input is received (top right). These subclasses form a two-layer processor in the CA3 recurrent circuit (bottom), potentially allowing parallel computations in the CA3 network. GC input (1) is predominantly received by sup PNs, which form a recurrent network (2) and project both downstream and into the second recurrent network of deep PNs (3). Specific innervation of each PN subclass by distinct interneurons may allow gating of information flow through each sublayer (black, 4).

See also Figure S5.

recorded cells, they apparently resulted from the activation of an unrecorded neuron presynaptic to two recorded neurons. Therefore, the timing of sPSCs can be used to infer the wiring of inputs onto recorded cells. Quantifying the percentage of events that are correlated between each cell pair revealed substantial shared input onto pairs of both superficial and deep PNs (3.4% ± 0.7% and 5.9% ± 0.7%, respectively). Simulation of random event timings showed that correlated events occurred significantly more often than expected by chance. Surprisingly, however, we did not observe such abundant coincident input onto cells of different classes (0.6% ± 0.2% synchronous; Figure 5B). These results suggest the existence of presynaptic neurons that preferentially wire into each PN subclass. Application of GABAzine substantially reduced the percentage of correlated events (Figure 5B). These results are consistent with subclass-specific inhibitory wiring in CA3, which could differentially control information flow through the two layers.

PN subclass-specific inhibition could occur either by receiving innervation from distinct interneuron subtypes or from individual interneurons. Biased innervation of deep and superficial PNs by distinct inhibitory cell types was described in hippocampal CA1.[15,17] To better characterize the source of subclass-specific inhibition, we applied pharmacological modulators of interneuron subtypes during multicellular recordings (1 µM WIN 55212-2 or 100 nM DAMGO[39]) and measured the abundance of correlated input to PN subtypes. sPSC frequencies were lower on deep than on superficial PNs in both conditions, as also seen without pharmacological manipulation (Figure S5B). Subtype-specific coincident input to PNs was observed in the presence of the cannabinoid receptor agonist WIN 55212-2 but not the µ-opioid receptor agonist DAMGO, with fewer correlated events on both superficial and deep PNs in the presence of DAMGO (Figure S5C). These data provide no evidence for differential wiring of interneuron subtypes into each PN subclass but implicate µ-opioid-sensitive interneurons in forming differential connections into each PN subclass. To further explore inhibitory innervation of PNs, we stained and imaged parvalbumin (PV) and cannabinoid receptor 1 (CB1R)-positive perisomatic axons in CA3 stratum pyramidale (Figure S5D). We observed a tendency for lower CB1R than PV innervation of deep CA3 somata in CA3, as was reported for CA1,[17] but not to an extent that would explain the structured input seen in correlated activity (Figures S5E and S5F). Together, our results are consistent with the hypothesis that individual inhibitory neurons preferentially innervate PN subtypes of the same class. While this hypothesis requires confirmation by further connectomic-style analysis, such a synaptic

arrangement would allow layer-specific control of recurrent circuit function, with the potential to powerfully gate information flow through the distinct sublayers of the CA3 network.

DISCUSSION

Our study reveals several unexpected properties of the hippocampal CA3 circuit. First, our results shed new light on the heterogeneity of PNs in CA3. Multiple studies have highlighted CA3 PN diversity on the deep-superficial axis. These include functional differences, with bursting and non-bursting cells,[22,24,37,40] but also morphological differences, such as long- and short-shaft PNs with differing mossy fiber input levels[21] or the timing of neuronal generation during brain development.[41] Consistent with recent results,[25] we demonstrate that deep neurons are a distinct subclass of CA3 PNs, with a burst-firing phenotype and sparse, but not absent, mossy-fiber input. This deep PN class includes morphologically identified athorny neurons,[23] but a complete lack of thorny excrescences is not a strict requirement for subclass identity, in line with other reports.[26] Genetic determination of how this deep subclass maps onto previously identified genetic divisions in CA3 sublayers[30,31] or how sparse PCP4+ cells in CA3 relate to this population[42] would be required for complete subclass characterization. Genetic profiling of CA3 demonstrated differential expression patterns for several genes between deep and superficial CA3 cells, including K+ channel expression, which may contribute to their specific firing phenotypes.[30,33] Deep and superficial layer organization is reminiscent of CA1, in which cell subtypes can be distinguished based on morphological properties, calbindin expression, and synaptic connectivity.[12,13,15,16,18,43–45] Thus, two-layer organization is a general principle that applies throughout the hippocampal formation.

Two-layer organization emerges partway along the CA3 proximal-distal axis, with the greatest abundance of deep PNs occurring in distal CA3 (see also Hunt et al.[23]). Multiple features differ between the first third (proximal) and remainder (distal) of the CA3 transverse axis. In addition to the presence of a deep PN layer, the infrapyramidal blade of the mossy fiber tract is lost, and increased innervation from the EC occurs in distal CA3.[5,46] In addition, the action potential phenotypes (this study and Sun et al.[29]) and dendritic Ca2+ spike properties of CA3 PNs[34] appear to switch at one-third of the CA3 transverse length, corresponding to proximal and distal subfields. Our data add another piece to the emerging picture of distinct microcircuit organization between proximal and distal CA3. Functionally, CA3 is considered to be important for higher-order computations, such as pattern separation and pattern completion.[7,47,48] Previous studies have suggested that these functions are divided between proximal and distal CA3,[49] while others have shown specific routing of non-spatial information through proximal CA3.[50] The switch in cell-type abundance, properties, and microcircuit connectivity across CA3 may contribute to the transformation of information processing between distinct CA3 subregions. Historically, CA3 has been subdivided into subfields a, b, and c. While CA3c corresponds to proximal CA3, our data provide no evidence to suggest further subdivision of distal CA3 into subfields a and b.

Our results reveal a striking asymmetry in hippocampal connectivity. This implies that CA3 is not a single recurrent network as previously assumed. Superficial and deep cells form intralayer recurrent networks, with minimal activity flow from deep to superficial PNs, at least at the level of local microcircuits. While superficial CA3 PNs are embedded in the classical trisynaptic circuit, forming an EC→GC→superficial CA3→CA1 multisynaptic loop, low DG input and asymmetric connectivity of deep CA3 cells imply a nested "tetrasynaptic" subcircuit: EC→GC→superficial CA3→deep CA3→CA1 (Figure 5C). Whether the output of this laminar CA3 processing follows into deep and superficial layers of CA1 will have major consequences for hippocampal information processing and must be explored in future studies. One caveat of multicellular patch-clamp-based circuit mapping is the focus on local connectivity. It is possible that deep-to-superficial connectivity exists but on a longer-distance scale. Such an arrangement could broadcast local CA3 dynamics for long-range coordination of network events across the broadly connected CA3 circuit.[27,51,52] Future work, for example, using transsynaptic labeling with rabies viruses,[53] will be needed to map the synaptic inputs and outputs of the two-layered CA3 microcircuits that we have identified. Previous work suggested a role for deep (athorny) PNs in coordinating network events, such as sharp-wave ripples.[23] Our finding of asymmetric connectivity suggests that this action does not occur through local recurrent activity of deep PNs; however, both longer-range connectivity and local disinhibitory mechanisms are possible.

The potential processing power of the microcircuit arrangement we observe is an interesting consideration. Ensembles of PNs in the CA3 recurrent system are thought to build and store our experiences.[54] Given that the deep PN layer will receive the output of these "completed" ensembles, their synaptic wiring has the potential to allow higher-order "associations of associations," akin to multilayer recurrent networks being used for artificial intelligence operations. In addition, the different input-output balance of deep and superficial PNs (Figure 5C) implies that ensemble size and activation threshold will likely differ between deep and superficial recurrent networks, further complexifying information processing.

The hippocampus is part of the allocortex, a phylogenetically old and highly conserved brain region. It is generally thought that the organization of the allocortex, with its 3-layered structure and its linear connectivity scheme, is much simpler than that of the neocortex, with its 6 layers and several overlapping canonical connectivity motifs.[55] Our results suggest that the hippocampal CA3 network and the canonical neocortical circuit might be more similar to each other than previously thought. Not only the presence of two layers throughout the hippocampal trisynaptic circuit but also the preferential connections from superficial to deep CA3 PNs are reminiscent of the neocortex.[55] Biased connectivity toward deeper neurons has been observed in both mouse subiculum[56,57] and within human neocortical layers.[58] Thus, while somatic density has been condensed in the allocortex, the circuit architectures of the allo- and neocortex may be more similar than appreciated.

Previous research demonstrated that deep PNs are the first to be generated in hippocampal development,[41] while in CA1,

neurons generated at the same developmental time point have been suggested to be preferentially connected to the same interneuron populations.[59] Our results are in line with these observations, indicating that deep and superficial PNs have preferential innervation from distinct interneurons. This appears to occur through the wiring of individual μ-opioid-sensitive interneurons (which include PV-positive basket cells) preferentially into either PN subclass, yet connectomic analysis is required to confirm such an arrangement. The topology of this inhibitory wiring gives inhibitory neurons the potential to differentially gate activity flow in the two layers, directing information flow through CA3. Therefore, identifying these interneuron populations and determining their complete integration into the CA3 microcircuit will further illuminate the complexity of the CA3 processor. Together, our results help to break down the view of a "simple" hippocampal circuit and begin to identify the microcircuit details, which are necessary to understand the rules of complex information processing in this important brain area.

Limitations of the study

This study focuses on local microcircuit properties; long-range connections will not be detected in slice tissue preparations. Whether local asymmetric connectivity applies to longer-range connections requires further investigation. In addition, exact connectivity values will be underestimated in the slice preparation (as discussed in Watson et al.[27]). Sparse connectivity in hippocampal circuits also limits the size of synaptic datasets, and greater diversity in synaptic properties may be revealed in future studies with larger datasets. In our work, analysis was performed at room temperature. While this may not affect the distinction between cell types, the exact firing properties of these cells will be different at physiological temperature and under *in vivo* conditions. Likewise, synaptic properties will differ at physiological temperature and may be shifted toward higher synaptic reliability and greater facilitation during train stimulation.[6,60,61] Finally, subclass-specific inhibitory innervation is the most parsimonious interpretation of our observations from correlated input patterns, but large-scale connectomic studies will be needed for a direct demonstration of the underlying circuit motifs.

RESOURCE AVAILABILITY

Lead contact
Requests for resources and reagents should be directed to Peter Jonas (peter.jonas@ist.ac.at).

Materials availability
This study did not generate new unique reagents.

Data and code availability
- All data reported in this paper will be shared by the lead contact upon request.
- All original code has been deposited at https://github.com/jakefwatson/patchanalysis and is publicly available at https://doi.org/10.5281/zenodo.15776965 as of the date of publication.
- Any additional information required to reanalyze the data reported in this paper is available from the lead contact upon request.

AUTHOR CONTRIBUTIONS

Conceptualization, J.F.W. and P.J.; methodology, all authors; experiments and analysis, J.F.W.; support with experiments and analysis, V.V.-B.; writing – original draft, J.F.W. and P.J.; writing – review & editing, all authors; funding acquisition, all authors; resources, all authors; supervision, P.J.

DECLARATION OF INTERESTS

The authors declare no competing interests.

STAR★METHODS

Detailed methods are provided in the online version of this paper and include the following:

- KEY RESOURCES TABLE
- EXPERIMENTAL MODEL AND STUDY PARTICIPANT DETAILS
  - Animals
- METHOD DETAILS
  - Acute slice preparation
  - Electrophysiology
  - Post-hoc morphological visualization
  - Immunohistochemistry of perisomatic innervation
  - Cell classification
- QUANTIFICATION AND STATISTICAL ANALYSIS

SUPPLEMENTAL INFORMATION

Supplemental information can be found online at https://doi.org/10.1016/j.celrep.2025.116080.

REFERENCES

1. Squire, L.R., Stark, C.E.L., and Clark, R.E. (2004). The medial temporal lobe. Annu. Rev. Neurosci. *27*, 279–306. https://doi.org/10.1146/annurev.neuro.27.070203.144130.

2. Squire, L.R. (2009). The legacy of patient H.M. for neuroscience. Neuron *61*, 6–9. https://doi.org/10.1016/j.neuron.2008.12.023.

3. Andersen, P., Bliss, T.V., and Skrede, K.K. (1971). Lamellar organization of hippocampal excitatory pathways. Exp. Brain Res. *13*, 222–238. https://doi.org/10.1007/BF00234087.

4. Amaral, D.G., and Witter, M.P. (1989). The three-dimensional organization of the hippocampal formation: A review of anatomical data. Neuroscience *31*, 571–591. https://doi.org/10.1016/0306-4522(89)90424-7.

5. Witter, M.P. (2007). Intrinsic and extrinsic wiring of CA3: Indications for connectional heterogeneity. Learn. Mem. *14*, 705–713. https://doi.org/10.1101/lm.725207.

6. Guzman, S.J., Schlögl, A., Frotscher, M., and Jonas, P. (2016). Synaptic mechanisms of pattern completion in the hippocampal CA3 network. Science *353*, 1117–1123. https://doi.org/10.1126/science.aaf1836.

7. Rolls, E.T. (2018). The storage and recall of memories in the hippocampo-cortical system. Cell Tissue Res. *373*, 577–604. https://doi.org/10.1007/s00441-017-2744-3.

8. Yeckel, M.F., and Berger, T.W. (1990). Feedforward excitation of the hippocampus by afferents from the entorhinal cortex: redefinition of the role of the trisynaptic pathway. Proc. Natl. Acad. Sci. USA *87*, 5832–5836. https://doi.org/10.1073/pnas.87.15.5832.

9. Ben-Simon, Y., Kaefer, K., Velicky, P., Csicsvari, J., Danzl, J.G., and Jonas, P. (2022). A direct excitatory projection from entorhinal layer 6b neurons to the hippocampus contributes to spatial coding and memory. Nat. Commun. *13*, 4826. https://doi.org/10.1038/s41467-022-32559-8.

10. Dudek, S.M., Alexander, G.M., and Farris, S. (2016). Rediscovering area CA2: unique properties and functions. Nat. Rev. Neurosci. *17*, 89–102. https://doi.org/10.1038/nrn.2015.22.

11. Cembrowski, M.S., and Spruston, N. (2019). Heterogeneity within classical cell types is the rule: lessons from hippocampal pyramidal neurons. Nat. Rev. Neurosci. *20*, 193–204. https://doi.org/10.1038/s41583-019-0125-5.

12. Lorente de Nó, R. (1934). Studies on the structure of the cerebral cortex. II. Continuation of the study of the ammonic system. J. Psychol. Neurol. *46*, 113–177.

13. Celio, M.R. (1990). Calbindin D-28k and parvalbumin in the rat nervous system. Neuroscience *35*, 375–475. https://doi.org/10.1016/0306-4522(90)90091-h.

14. Slomianka, L., Amrein, I., Knuesel, I., Sørensen, J.C., and Wolfer, D.P. (2011). Hippocampal pyramidal cells: the reemergence of cortical lamination. Brain Struct. Funct. *216*, 301–317. https://doi.org/10.1007/s00429-011-0322-0.

15. Lee, S.-H., Marchionni, I., Bezaire, M., Varga, C., Danielson, N., Lovett-Barron, M., Losonczy, A., and Soltesz, I. (2014). Parvalbumin-positive basket cells differentiate among hippocampal pyramidal cells. Neuron *82*, 1129–1144. https://doi.org/10.1016/j.neuron.2014.03.034.

16. Mizuseki, K., Diba, K., Pastalkova, E., and Buzsáki, G. (2011). Hippocampal CA1 pyramidal cells form functionally distinct sublayers. Nat. Neurosci. *14*, 1174–1181. https://doi.org/10.1038/nn.2894.

17. Valero, M., Cid, E., Averkin, R.G., Aguilar, J., Sanchez-Aguilera, A., Viney, T.J., Gomez-Dominguez, D., Bellistri, E., and de la Prida, L.M. (2015). Determinants of different deep and superficial CA1 pyramidal cell dynamics during sharp-wave ripples. Nat. Neurosci. *18*, 1281–1290. https://doi.org/10.1038/nn.4074.

18. Danielson, N.B., Zaremba, J.D., Kaifosh, P., Bowler, J., Ladow, M., and Losonczy, A. (2016). Sublayer-specific coding dynamics during spatial navigation and learning in hippocampal area CA1. Neuron *91*, 652–665. https://doi.org/10.1016/j.neuron.2016.06.020.

19. Geiller, T., Fattahi, M., Choi, J.-S., and Royer, S. (2017). Place cells are more strongly tied to landmarks in deep than in superficial CA1. Nat. Commun. *8*, 14531. https://doi.org/10.1038/ncomms14531.

20. Esparza, J., Quintanilla, J.P., Cid, E., Medeiros, A.C., Gallego, J.A., and de la Prida, L.M. (2025). Cell-type-specific manifold analysis discloses independent geometric transformations in the hippocampal spatial code. Neuron *113*, 1098–1109.e6. https://doi.org/10.1016/j.neuron.2025.01.022.

21. Fitch, J.M., Juraska, J.M., and Washington, L.W. (1989). The dendritic morphology of pyramidal neurons in the rat hippocampal CA3 area. I. Cell types. Brain Res. *479*, 105–114. https://doi.org/10.1016/0006-8993(89)91340-1.

22. Bilkey, D.K., and Schwartzkroin, P.A. (1990). Variation in electrophysiology and morphology of hippocampal CA3 pyramidal cells. Brain Res. *514*, 77–83. https://doi.org/10.1016/0006-8993(90)90437-G.

23. Hunt, D.L., Linaro, D., Si, B., Romani, S., and Spruston, N. (2018). A novel pyramidal cell type promotes sharp-wave synchronization in the hippocampus. Nat. Neurosci. *21*, 985–995. https://doi.org/10.1038/s41593-018-0172-7.

24. Raus Balind, S., Magó, Á., Ahmadi, M., Kis, N., Varga-Németh, Z., Lőrincz, A., and Makara, J.K. (2019). Diverse synaptic and dendritic mechanisms of complex spike burst generation in hippocampal CA3 pyramidal cells. Nat. Commun. *10*, 1859. https://doi.org/10.1038/s41467-019-09767-w.

25. Magó, Á., Kis, N., Lükő, B., and Makara, J.K. (2021). Distinct dendritic Ca^{2+} spike forms produce opposing input-output transformations in rat CA3 pyramidal cells. eLife *10*, e74493. https://doi.org/10.7554/eLife.74493.

26. Balleza-Tapia, H., Arroyo-García, L.E., Isla, A.G., Loera-Valencia, R., and Fisahn, A. (2022). Functionally-distinct pyramidal cell subpopulations during gamma oscillations in mouse hippocampal area CA3. Prog. Neurobiol. *210*, 102213. https://doi.org/10.1016/j.pneurobio.2021.102213.

27. Watson, J.F., Vargas-Barroso, V., Morse-Mora, R.J., Navas-Olive, A., Tavakoli, M.R., Danzl, J.G., Tomschik, M., Rössler, K., and Jonas, P. (2025). Human hippocampal CA3 uses specific functional connectivity rules for efficient associative memory. Cell *188*, 501–514.e18. https://doi.org/10.1016/j.cell.2024.11.022.

28. Kowalski, J., Gan, J., Jonas, P., and Pernía-Andrade, A.J. (2016). Intrinsic membrane properties determine hippocampal differential firing pattern in vivo in anesthetized rats. Hippocampus *26*, 668–682. https://doi.org/10.1002/hipo.22550.

29. Sun, Q., Sotayo, A., Cazzulino, A.S., Snyder, A.M., Denny, C.A., and Siegelbaum, S.A. (2017). Proximodistal heterogeneity of hippocampal CA3 pyramidal neuron intrinsic properties, connectivity, and reactivation during memory recall. Neuron *95*, 656–672.e3. https://doi.org/10.1016/j.neuron.2017.07.012.

30. Thompson, C.L., Pathak, S.D., Jeromin, A., Ng, L.L., MacPherson, C.R., Mortrud, M.T., Cusick, A., Riley, Z.L., Sunkin, S.M., Bernard, A., et al. (2008). Genomic anatomy of the hippocampus. Neuron *60*, 1010–1021. https://doi.org/10.1016/j.neuron.2008.12.008.

31. Yao, Z., van Velthoven, C.T.J., Nguyen, T.N., Goldy, J., Sedeno-Cortes, A.E., Baftizadeh, F., Bertagnolli, D., Casper, T., Chiang, M., Crichton, K., et al. (2021). A taxonomy of transcriptomic cell types across the isocortex and hippocampal formation. Cell *184*, 3222–3241.e26. https://doi.org/10.1016/j.cell.2021.04.021.

32. Vandael, D., and Jonas, P. (2024). Structure, biophysics, and circuit function of a "giant" cortical presynaptic terminal. Science *383*, eadg6757. https://doi.org/10.1126/science.adg6757.

33. Linaro, D., Levy, M.J., and Hunt, D.L. (2022). Cell type-specific mechanisms of information transfer in data-driven biophysical models of hippocampal CA3 principal neurons. PLoS Comput. Biol. *18*, e1010071. https://doi.org/10.1371/journal.pcbi.1010071.

34. Kis, N., Lükő, B., Herédi, J., Magó, Á., Erlinghagen, B., Ahmadi, M., Raus Balind, S., Irás, M., Ujfalussy, B.B., and Makara, J.K. (2024). Cholinergic regulation of dendritic Ca^{2+} spikes controls firing mode of hippocampal CA3 pyramidal neurons. Proc. Natl. Acad. Sci. *121*, e2321501121. https://doi.org/10.1073/pnas.2321501121.

35. Sammons, R.P., Vezir, M., Moreno-Velasquez, L., Cano, G., Orlando, M., Sievers, M., Grasso, E., Metodieva, V.D., Kempter, R., Schmidt, H., and Schmitz, D. (2024). Structure and function of the hippocampal CA3 module. Proc. Natl. Acad. Sci. USA *121*, e2312281120. https://doi.org/10.1073/pnas.2312281120.

36. Miles, R., and Wong, R.K. (1986). Excitatory synaptic interactions between CA3 neurones in the guinea-pig hippocampus. J. Physiol. *373*, 397–418. https://doi.org/10.1113/jphysiol.1986.sp016055.

37. Hemond, P., Epstein, D., Boley, A., Migliore, M., Ascoli, G.A., and Jaffe, D.B. (2008). Distinct classes of pyramidal cells exhibit mutually exclusive

firing patterns in hippocampal area CA3b. Hippocampus *18*, 411–424. https://doi.org/10.1002/hipo.20404.

38. Rieubland, S., Roth, A., and Häusser, M. (2014). Structured connectivity in cerebellar inhibitory networks. Neuron *81*, 913–929. https://doi.org/10.1016/j.neuron.2013.12.029.

39. Glickfeld, L.L., Atallah, B.V., and Scanziani, M. (2008). Complementary modulation of somatic inhibition by opioids and cannabinoids. J. Neurosci. *28*, 1824–1832. https://doi.org/10.1523/JNEUROSCI.4700-07.2008.

40. Masukawa, L.M., Benardo, L.S., and Prince, D.A. (1982). Variations in electrophysiological properties of hippocampal neurons in different subfields. Brain Res. *242*, 341–344. https://doi.org/10.1016/0006-8993(82)90320-1.

41. Marissal, T., Bonifazi, P., Picardo, M.A., Nardou, R., Petit, L.F., Baude, A., Fishell, G.J., Ben-Ari, Y., and Cossart, R. (2012). Pioneer glutamatergic cells develop into a morpho-functionally distinct population in the juvenile CA3 hippocampus. Nat. Commun. *3*, 1316. https://doi.org/10.1038/ncomms2318.

42. Fernandez-Lamo, I., Gomez-Dominguez, D., Sanchez-Aguilera, A., Oliva, A., Morales, A.V., Valero, M., Cid, E., Berenyi, A., and de la Prida, L.M. (2019). Proximodistal organization of the CA2 hippocampal area. Cell Rep. *26*, 1734–1746.e6. https://doi.org/10.1016/j.celrep.2019.01.060.

43. Navas-Olive, A., Valero, M., Jurado-Parras, T., de Salas-Quiroga, A., Averkin, R.G., Gambino, G., Cid, E., and de la Prida, L.M. (2020). Multimodal determinants of phase-locked dynamics across deep-superficial hippocampal sublayers during theta oscillations. Nat. Commun. *11*, 2217. https://doi.org/10.1038/s41467-020-15840-6.

44. Soltesz, I., and Losonczy, A. (2018). CA1 pyramidal cell diversity enabling parallel information processing in the hippocampus. Nat. Neurosci. *21*, 484–493. https://doi.org/10.1038/s41593-018-0118-0.

45. Morris, M.E., Baimbridge, K.G., El-Beheiry, H., Obrocea, G.V., and Rosen, A.S. (1995). Correlation of anoxic neuronal responses and calbindin-D$_{28k}$ localization in stratum pyramidale of rat hippocampus. Hippocampus *5*, 25–39. https://doi.org/10.1002/hipo.450050105.

46. Ishizuka, N., Cowan, W.M., and Amaral, D.G. (1995). A quantitative analysis of the dendritic organization of pyramidal cells in the rat hippocampus. J. Comp. Neurol. *362*, 17–45. https://doi.org/10.1002/cne.903620103.

47. Nakashiba, T., Young, J.Z., McHugh, T.J., Buhl, D.L., and Tonegawa, S. (2008). Transgenic inhibition of synaptic transmission reveals role of CA3 output in hippocampal learning. Science *319*, 1260–1264. https://doi.org/10.1126/science.1151120.

48. Guzman, S.J., Schlögl, A., Espinoza, C., Zhang, X., Suter, B.A., and Jonas, P. (2021). How connectivity rules and synaptic properties shape the efficacy of pattern separation in the entorhinal cortex–dentate gyrus–CA3 network. Nat. Comput. Sci. *1*, 830–842. https://doi.org/10.1038/s43588-021-00157-1.

49. Lee, H., Wang, C., Deshmukh, S.S., and Knierim, J.J. (2015). Neural population evidence of functional heterogeneity along the CA3 transverse axis: pattern completion versus pattern separation. Neuron *87*, 1093–1105. https://doi.org/10.1016/j.neuron.2015.07.012.

50. Nakamura, N.H., Flasbeck, V., Maingret, N., Kitsukawa, T., and Sauvage, M.M. (2013). Proximodistal segregation of nonspatial information in CA3: Preferential recruitment of a proximal CA3-distal CA1 network in nonspatial recognition memory. J. Neurosci. *33*, 11506–11514. https://doi.org/10.1523/JNEUROSCI.4480-12.2013.

51. Ishizuka, N., Weber, J., and Amaral, D.G. (1990). Organization of intrahippocampal projections originating from CA3 pyramidal cells in the rat. J. Comp. Neurol. *295*, 580–623. https://doi.org/10.1002/cne.902950407.

52. Li, X.G., Somogyi, P., Ylinen, A., and Buzsáki, G. (1994). The hippocampal CA3 network: An in vivo intracellular labeling study. J. Comp. Neurol. *339*, 181–208. https://doi.org/10.1002/cne.903390204.

53. Sumser, A., Joesch, M., Jonas, P., and Ben-Simon, Y. (2022). Fast, high-throughput production of improved rabies viral vectors for specific, efficient and versatile transsynaptic retrograde labeling. eLife *11*, e79848. https://doi.org/10.7554/eLife.79848.

54. Treves, A., and Rolls, E.T. (1994). Computational analysis of the role of the hippocampus in memory. Hippocampus *4*, 374–391. https://doi.org/10.1002/hipo.450040319.

55. Douglas, R.J., and Martin, K.A.C. (2004). Neuronal circuits of the neocortex. Annu. Rev. Neurosci. *27*, 419–451. https://doi.org/10.1146/annurev.neuro.27.070203.144152.

56. Funahashi, M., and Stewart, M. (1997). Presubicular and parasubicular cortical neurons of the rat: functional separation of deep and superficial neurons in vitro. J. Physiol. *501*, 387–403. https://doi.org/10.1111/j.1469-7793.1997.387bn.x.

57. Peng, Y., Barreda Tomás, F.J., Klisch, C., Vida, I., and Geiger, J.R.P. (2017). Layer-specific organization of local excitatory and inhibitory synaptic connectivity in the rat presubiculum. Cereb. Cortex *27*, 2435–2452. https://doi.org/10.1093/cercor/bhx049.

58. Peng, Y., Bjelde, A., Aceituno, P.V., Mittermaier, F.X., Planert, H., Grosser, S., Onken, J., Faust, K., Kalbhenn, T., Simon, M., et al. (2024). Directed and acyclic synaptic connectivity in the human layer 2-3 cortical microcircuit. Science *384*, 338–343. https://doi.org/10.1126/science.adg8828.

59. Huszár, R., Zhang, Y., Blockus, H., and Buzsáki, G. (2022). Preconfigured dynamics in the hippocampus are guided by embryonic birthdate and rate of neurogenesis. Nat. Neurosci. *25*, 1201–1212. https://doi.org/10.1038/s41593-022-01138-x.

60. Hardingham, N.R., and Larkman, A.U. (1998). The reliability of excitatory synaptic transmission in slices of rat visual cortex in vitro is temperature dependent. J. Physiol. *507*, 249–256. https://doi.org/10.1111/j.1469-7793.1998.249bu.x.

61. Pyott, S.J., and Rosenmund, C. (2002). The effects of temperature on vesicular supply and release in autaptic cultures of rat and mouse hippocampal neurons. J. Physiol. *539*, 523–535. https://doi.org/10.1113/jphysiol.2001.013277.

62. Tamamaki, N., Yanagawa, Y., Tomioka, R., Miyazaki, J.-I., Obata, K., and Kaneko, T. (2003). Green fluorescent protein expression and colocalization with calretinin, parvalbumin, and somatostatin in the GAD67-GFP knock-in mouse. J. Comp. Neurol. *467*, 60–79. https://doi.org/10.1002/cne.10905.

63. Guzman, S.J., Schlögl, A., and Schmidt-Hieber, C. (2014). Stimfit: quantifying electrophysiological data with Python. Front. Neuroinformatics *8*, 16. https://doi.org/10.3389/fninf.2014.00016.

64. Feng, L., Zhao, T., and Kim, J. (2015). neuTube 1.0: A new design for efficient neuron reconstruction software based on the SWC format. eNeuro *2*, 0049-14.2014. https://doi.org/10.1523/ENEURO.0049-14.2014.

65. Schindelin, J., Arganda-Carreras, I., Frise, E., Kaynig, V., Longair, M., Pietzsch, T., Preibisch, S., Rueden, C., Saalfeld, S., Schmid, B., et al. (2012). Fiji - an open source platform for biological image analysis. Nat. Methods *9*, 676–682. https://doi.org/10.1038/nmeth.2019.

66. Hosp, J.A., Strüber, M., Yanagawa, Y., Obata, K., Vida, I., Jonas, P., and Bartos, M. (2014). Morpho-physiological criteria divide dentate gyrus interneurons into classes. Hippocampus *24*, 189–203. https://doi.org/10.1002/hipo.22214.

67. Bischofberger, J., Engel, D., Li, L., Geiger, J.R.P., and Jonas, P. (2006). Patch-clamp recording from mossy fiber terminals in hippocampal slices. Nat. Protoc. *1*, 2075–2081. https://doi.org/10.1038/nprot.2006.312.

68. Jonas, P., Major, G., and Sakmann, B. (1993). Quantal components of unitary EPSCs at the mossy fibre synapse on CA3 pyramidal cells of rat hippocampus. J. Physiol. *472*, 615–663. https://doi.org/10.1113/jphysiol.1993.sp019965.

69. Clements, J.D., and Bekkers, J.M. (1997). Detection of spontaneous synaptic events with an optimally scaled template. Biophys. J. *73*, 220–229. https://doi.org/10.1016/S0006-3495(97)78062-7.

70. Greger, I.H., and Watson, J.F. (2024). 'Mini analysis' is an unreliable reporter of synaptic changes. Preprint at bioRxiv. https://doi.org/10.1101/2024.10.26.620084.

71. Tainaka, K., Kubota, S.I., Suyama, T.Q., Susaki, E.A., Perrin, D., Ukai-Tadenuma, M., Ukai, H., and Ueda, H.R. (2014). Whole-body imaging with single-cell resolution by tissue decolorization. Cell *159*, 911–924. https://doi.org/10.1016/j.cell.2014.10.034.

STAR★METHODS

KEY RESOURCES TABLE

REAGENT or RESOURCE	SOURCE	IDENTIFIER
Antibodies		
Rabbit polyclonal anti-NeuN	Thermo Fisher Scientific	PA5-37407, RRID:AB_2554049
Guinea-pig polyclonal anti-NeuN	Millipore	Cat# ABN90, RRID:AB_11205592
Rabbit polyclonal anti-CB1R	Cayman Chemical	Cat# 10006590; RRID:AB_10098690
Rabbit polyclonal anti-parvalbumin	Swant	Cat# PV25, RRID:AB_10000344
Goat AF488-conjugated anti-guinea-pig secondary	Thermo Fisher Scientific	Cat# A-11073, RRID:AB_2534117
Goat AF594-conjugated anti-rabbit secondary	Thermo Fisher Scientific	Cat# A-11037, RRID:AB_2534095
Goat AF488-conjugated anti-rabbit secondary	Thermo Fisher Scientific	A11034, RRID:AB_2576217
Chemicals, peptides, and recombinant proteins		
Biocytin	Invitrogen	#B1592
Paraformaldehyde (PFA)	TAAB	P001/2
AF647-conjugated streptavidin	Invitrogen	S32357
Mowiol 4-88	Carl Roth	713.2
Vectastain Elite ABC HRP-Kit	Vector Laboratories	PK-6100
DAB, 3,3′-Diaminobenzidine-tetrahydrochlorid Hydrate	Sigma-Aldrich	D5637-5G
GABAzine (SR-95531 hydrobromide)	Biotrend AG	BN0507
$NiCl_2$	Sigma-Aldrich	223387-25G
$CoCl_2$	Sigma-Aldrich	C8661-25G
3,3′-diaminobenzidine	Sigma-Aldrich	D5637-5G
2,2′,2″,-nitrilotriethanol	Sigma-Aldrich	90279
(R)-(+)-WIN 55,212-2 mesylate salt	Merck	W102
DAMGO	Merck	E7384
Deposited data		
Custom code for data analysis	This study	Zenodo deposit: 10.5281/zenodo.15776965
Experimental models: Organisms/strains		
Mouse: C57BL/6J	The Jackson Laboratory	RRID: IMSR_JAX000664
Mouse: GAD67-EGFP	Provided by K. Obata	Tamamaki et al.[62]
Software and algorithms		
Stimfit v.0.15.8	Guzman et al.[63]	https://github.com/neurodroid/stimfit
Signal v.6.0	CED	https://ced.co.uk/products/signal
Matlab R2022b	Mathworks	https://de.mathworks.com/products/matlab.html
Imaris Stitcher Software	Oxford Instruments	https://imaris.oxinst.com/products/imaris-stitcher
Neutube analysis software	Feng et al.[64]	https://neutracing.com/
FIJI/ImageJ	Schindelin et al.[65]	https://fiji.sc/
GraphPad Prism v.10.2.2	GraphPad	https://www.graphpad.com/features
Other		
Borosilicate glass tubing	Hilgenberg	1807542

EXPERIMENTAL MODEL AND STUDY PARTICIPANT DETAILS

Animals

All procedures were performed in strict accordance with institutional, national, and European guidelines for animal experimentation, approved by the Bundesministerium für Bildung, Wissenschaft und Forschung of Austria. Wild-type C57BL/6J mice (RRID:IMSR_ JAX:000664) or GAD67-EGFP mice (provided by K. Obata, see[62,66]) of both sexes were used at postnatal (P) day 20–30 (median age: P23). A subset of recordings was performed with wild-type animals at postnatal age of 6–7 weeks. All animals were housed

with *ad libitum* access to food and water, with constant temperature (22°C) and humidity (50–60%), under a 12-h light-dark cycle, and used for experiments during the light phase.

METHOD DETAILS

Acute slice preparation

Animals were sacrificed by decapitation under light isoflurane anesthesia. Brains were extracted rapidly in ice-cold high-sucrose artificial cerebrospinal fluid (aCSF, containing either: 64 mM NaCl, 25 mM NaHCO$_3$, 2.5 mM KCl, 1.25 mM NaH$_2$PO$_4$, 10 mM D-glucose, 120 mM sucrose, 7 mM MgCl$_2$, and 0.5 mM CaCl at osmolarity ~334 mOsm; or 87 mM NaCl, 25 mM NaHCO$_3$, 2.5 mM KCl, 1.25 mM NaH$_2$PO$_4$, 10 mM D-glucose, 75 mM sucrose, 7 mM MgCl$_2$, and 0.5 mM CaCl$_2$ at osmolarity ~325 mOsm), equilibrated with 95% O$_2$ and 5% CO$_2$ gas mixture (carbogen). Hemispheres were separated by a single sagittal cut using a scalpel blade. Acute slices were cut using transverse or quasi-transverse preparation[67] unless otherwise stated, and glued to a specimen plate using liquid superglue (UHU, 45570). 350-μm-thick slices were cut with a VT 1200 vibratome (Leica Microsystems). Slices were then transferred to a recovery chamber containing either high-sucrose aCSF, or recording aCSF (containing 125 mM NaCl, 25 mM NaHCO$_3$, 2.5 mM KCl, 1.25 mM NaH$_2$PO$_4$, 25 mM D-glucose, 2 mM CaCl$_2$, and 1 mM MgCl$_2$, osmolarity ~317 mOsm) at 35°C for 30–45 min with continuous carbogen bubbling, before maintenance in this solution at room temperature (RT, 20°C–22°C) until recording. Due to the quasi-transverse preparation, the majority of recordings were performed from mid-ventral hippocampus. A small dataset was acquired from the dorsal hippocampus, using the same cutting conditions as previously, however "quasi-coronally". In this approach, the cerebellum was removed and hemispheres were separated. Next, a blocking cut was made to the posterior of the brain at approximately 30°–40° with respect to the cortex-cerebellar boundary, and the brain was glued to the specimen plate on this newly cut surface. This approach allows slicing perpendicular to the longitudinal axis of the dorsal hippocampus, and minimizes the extent of CA3 dendrite severance when compared to classical coronal slicing. For animals used at postnatal age 6–7 weeks, quasi-transverse slices were prepared as above, except that animals were deeply anesthetized by injection of MMF (0.3 mg kg^{-1} medetomidine (Dormitor; Pfizer), 8 mg kg^{-1} midazolam (Dormicum; Roche), and 0.01 mg kg^{-1} fentanyl (Piramal Critical Care)) before transcardial perfusion with 10–15 mL of ice-cold high-sucrose aCSF prior to decapitation and brain extraction.

Electrophysiology

Slices were transferred to the recording chamber, and continuously perfused with aCSF bubbled with carbogen. Slices were held in place with a platinum harp with nylon threads to prevent tissue movement during recordings. Patch-clamp recording pipettes were pulled from thick-walled borosilicate glass tubing (Hilgenberg, 2 mm OD, 1 mm ID, 1807542), and filled with intracellular solution (containing 135 mM K gluconate, 20 mM KCl, 0.1 mM EGTA, 2 mM MgCl$_2$, 2 mM Na$_2$ATP, 0.3 mM NaGTP, and 10 mM HEPES, adjusted to pH 7.28 with KOH; osmolarity ~302 mOsm, with 0.2% (w/v) biocytin). Micropipettes had open tip resistances of 2–6 MΩ when filled with internal solution, and were positioned manually using eight Junior 20ZR micromanipulators (Luigs and Neumann). Neurons were targeted using infrared differential interference contrast (IR-DIC) videomicroscopy based on their soma location in the CA3 pyramidal cell layer. Electrical signals were recorded using four Multiclamp 700B amplifiers (Molecular Devices), low-pass filtered at 6–10 kHz with built-in Bessel filters, and digitized at 20 kHz with a Power 1401 data acquisition interface (Cambridge Electronic Design). Protocols were generated and applied using Signal 6.0 software (Cambridge Electronic Design). All experiments were performed at 21°C (range: 20°C–22°C).

Pipette offset and capacitance were measured and accounted for during all recordings. During current-clamp recordings, pipette capacitance was ~70% compensated in all cases, and series resistance compensation was applied as appropriate. Neuronal firing properties were assessed by injection of 1-s hyperpolarizing or depolarizing currents in 50 pA steps (−100 to 400 pA range). Synaptic connectivity was tested by eliciting action potentials (APs) in each recorded neuron in current-clamp mode in turn, while recording responses from all other neurons in either current- or voltage-clamp configurations. APs were elicited by brief current injection (2–5 ms) at a level sufficient to reliably evoke single spikes (typically 1–2 nA). Connectivity was routinely tested by stimulation with 5 APs at 20 Hz, repeated at least 40 times. Monosynaptic connections were identified by reliable appearance of synaptic responses in the average trace across all pulses of 20 Hz stimulation, with a short latency between presynaptic AP peak and response onset (<4 ms). Electrical coupling was tested by injection of a 50-pA hyperpolarizing current for 250 ms to the presynaptic cell, and monitoring responses in all other cells. No electrical coupling was observed between CA3 PNs. After recordings, pipettes were slowly retracted from the cell somata to form outside-out patches, which ensured retention of intracellular biocytin for post-hoc staining. The quality of patch formation and the physical location of recorded cells in the tissue slice were documented for later cell identification in stained tissue. Recorded traces were analyzed using Stimfit (version v0.15.8[63]) or custom MATLAB scripts (available at https://github.com/jakefwatson/patchanalysis; version of record: https://doi.org/10.5281/zenodo.15776965). Cells with a membrane potential above −50 mV or requiring current injection to maintain V$_m$ below −50 mV were excluded from analysis of passive and active properties. Cell properties were tested immediately after achieving the whole-cell configuration. Resting membrane potential was measured as the median V$_m$ without current injection (0 pA injection step of firing characterization), input resistance was calculated from the end of −100, −50, and +50 pA injections (median voltages between 0.65 and 0.95 s of 1-s pulses). Rheobase current was the required injection for first spike generation

during 50-pA step injections. Maximum bursting frequency was defined as the highest instantaneous frequency of the first two spikes upon current injection at either 350 or 400 pA steps. Initial interspike interval (ISI) was defined as the minimal ISI from the first two sweeps generating at least two spikes. Spike-frequency adaptation (SFA) was measured from the first sweep with at least five APs calculated by dividing the mean of the first two ISIs by the mean of the last two ISIs (a value of 1 therefore represents non-adapting spike frequencies, while values closer to 0 are more adapting). All voltage-clamp recordings were performed with a holding potential of -70 mV. Evoked synaptic successes were defined as sweeps with responses of consistent latency, with peak amplitudes exceeding 2.5 σ (EPSCs) or 3 σ (EPSPs) of baseline noise measured immediately prior to AP generation. Synaptic current rise times are between 20 and 80% of maximal response, while decay kinetics are time constant of a monoexponential fit offset to baseline values. Voltage-clamp synaptic responses were only analyzed in pairs with a postsynaptic access resistance of less than 20 MΩ.

sPSCs were recorded for at least 5 min, monitoring voltage-clamp conditions with a test pulse at least every 20 s. Cells that had an access resistance above 20 MΩ were discarded. Events were detected using a template-based analysis (minidet.m, Biosig toolbox, http://biosig.sf.net/; see[68,69]), and event times were measured as event onset. The standard deviation of recording noise was measured from 200-ms windows without visible spontaneous events, and was compared between conditions to ensure that differences in event frequency result from physiological effects, and not from altered event detection.[70] Crosscorrelograms were plotted by calculation of interevent intervals between all detected events of each cell, and all detected events of other recorded cells. "Correlated events" were defined as events with onset times within 0.5 ms of one another (correlation window = event onset ±0.5 ms). The percentage of correlated events between each pair of recorded neurons was calculated for both cells of the pair. To confirm correlated event observation was not a result of by-chance superposition, the expected random correlated event frequency was simulated by randomization of event times for each cell and recalculation of correlated event percentages for each pair. The median of 100 simulation runs was presented. sEPSCs were pharmacologically isolated by application of 10 μM GABAzine (Biotrend AG) to aCSF. In subsequent analysis, multicellular recordings were performed with interleaved application of either 1 μM WIN 55212-2 ((R)-(+)-WIN 55,212-2 mesylate salt; Merck W102) or 100 nM DAMGO ([D-Ala2, N-Me-Phe4, Gly5-ol]-Enkephalin acetate salt; Merck E7384) immediately after cell spiking characterization, and correlated event analysis was performed as previously described. To ensure analyzed events did not arise from coordinated network activity rather than individual cell action, the percentage of correlated events that occurred simultaneously at 3 or more recorded cells was calculated, and recordings in which >10% of correlated events exhibited such activity were excluded.

A subset of recorded CA3 PNs from this dataset (1272 tested connections) was included in a previous study for cross-species connectivity comparison.[27]

Post-hoc morphological visualization

After recording, all slices were fixed and stained for intracellular biocytin to assess neuronal morphology. Slices were routinely imaged using 3,3′-diaminobenzidine (DAB) as chromogen; however a subset of slices were imaged using fluorescence-labeling. For DAB staining (Vectastain ABC-Elite Standard kit, Vector Laboratories PK-6100), slices were fixed in a solution containing 2.5% paraformaldehyde (PFA, TAAB Laboratories Equipment), 1.25% glutaraldehyde (GA; Carl Roth, 4157.1), and 15% (v/v) saturated picric acid solution (Sigma-Aldrich, P6744-1GA). After washing with phosphate buffer (PB; 0.1 M NaH_2PO_4 and 0.1 M Na_2HPO_4, Merck; titrated to pH 7.35), samples were treated with hydrogen peroxide (1%, 10 min; Sigma-Aldrich, 95321-100mL), permeabilized with 2% Triton X-100 (in PB, Sigma-Aldrich) for 1 h, and transferred to a solution containing 1% avidin-conjugated horseradish peroxidase complex and 1% Triton X-100 for ~12 h. After rinsing in 0.1 M PB, slices were incubated with a solution containing 0.036% DAB (Sigma-Aldrich, D5637-5G), 0.006% $NiCl_2$ (Sigma-Aldrich, 223387-25G) and 0.008% $CoCl_2$ (Sigma-Aldrich, C8661-25G), and developed by addition of 0.01% hydrogen peroxide. DAB-developed slices were mounted in Mowiol and cured for at least 24 h, before visualization using an Olympus BX61 widefield microscope. Recorded cells were visualized using 4, 10, or 20× objectives.

For fluorescent labeling, slices were fixed with 4% (w/v) paraformaldehyde (PFA) in 0.1 M PB at 4°C and washed in 0.1 M PB after 24 h to stop the fixation reaction. Slices were blocked and permeabilized by incubation with a solution containing 5% natural goat serum (NGS; Biozol ENG9010-10) and 0.4% Triton X-100 in 0.1 M PB for 2–3 h at RT. Alexa Fluor (AF) 647-conjugated streptavidin (1:300 diluted from 2 mg mL^{-1} stock solution, Invitrogen S32357) was added, and incubated overnight in blocking/permeabilizing solution at RT with gentle shaking. Samples were then washed in 0.1 M PB (3 × 30 min), before incubation with DAPI (4′,6-diamidino-2-phenylindole, dilactate, 0.1 μg mL^{-1} final concentration in PB, Invitrogen D3571) in 0.1 M PB for 10–20 min at RT. For dorsal CA3 recordings, all neurons were visualized by additional staining with anti-NeuN (overnight incubation; diluted 1:300 from stock; rabbit anti-NeuN, Thermo Fisher Scientific PA5-37407, RRID:AB_2554049), and subsequent visualization with AF488-conjugated anti-rabbit secondary antibody (overnight incubation; 1:300 from stock; goat anti rabbit AF488, Thermo Fisher Scientific A11034, RRID:AB_2576217) alongside streptavidin staining in the same solutions. Recorded slices were cleared by incubation for 10 min at RT in CUBIC solution[71] (50% sucrose, 25% urea, 10% 2,2′,2″,-nitrilotriethanol, 0.1% and Triton X-100 in MilliQ water; all Sigma-Aldrich: 16104, U5128-500G, 90279-100mL), before mounting on glass slides (Assistant, Karl Hecht ref. 42406020) beneath a 1.5 thickness glass coverslip (VWR 631-0147) in CUBIC solution surrounded by a ring of Mowiol (Mowiol 4–88, Carl Roth, 713,2; Glycerol, Sigma-Aldrich, G-9012) to prevent exposure of CUBIC solution to air. Samples were cured for at least 24 h prior to imaging. Slides were imaged on an ANDOR Dragonfly microscope (Oxford Instruments) equipped with a Zyla 4.2 Megapixel sCMOS camera

(2048 × 2048 pixels), using either a 10× air objective (Nikon MRD00105, CFI P-Apo 10×, NA 0.45) or a 20× water-immersion objective (Nikon MRD77200, CFI P-Apochromat 20×, NA 0.95). A pinhole disc with 25 μm hole diameter was used. Tiles were stitched using Imaris Stitcher software (Oxford Instruments). Axon reconstructions were performed using Neutube analysis software.[64]

Intersomatic distances were calculated as Euclidean distance between somatic centers in three dimensions. Proximal-distal distance dependence to connectivity and somatic location on this axis was measured by manual segmentation of *stratum pyramidale* as a vector to the end of *stratum lucidum* (from 4× images), and determination of somatic location along this vector. Somatic depth was taken as the distance between somatic center and the upper bound of *stratum lucidum*.

Immunohistochemistry of perisomatic innervation

Three mice aged P23–P25 were deeply anesthetized with first isoflurane inhalation (4% v/v), then MMF injection, before transcardial perfusion fixation with 4% PFA in 0.1 M PB. Brains were cut in the transverse plane using a VT 1200 vibratome (Leica Microsystems) into 100-μm-thick sections which were blocked and permeabilized by incubation with solution containing 5% natural goat serum and 0.4% Triton X-100 in 0.1 M PB for 2–3 h at RT, before overnight incubation with primary antibodies in the same solution at RT under gentle agitation. Primary antibodies were either anti-CB1R (rabbit; Cayman Chemical Cat# 10006590; RRID:AB_10098690), or anti-parvalbumin (rabbit; Swant Cat# PV 25, RRID:AB_10000344), paired with anti-NeuN (guinea-pig; Millipore Cat# ABN90, RRID: AB_11205592), all used at 1:500 dilution. Sections were washed thoroughly by multiple solution exchanges with agitation over 2 h in 0.1 M PB, before overnight incubation with secondary antibodies in blocking/permeabilization solution. Secondary antibodies were AF488-conjugated goat anti-guinea-pig (Thermo Fisher Scientific Cat# A-11073, RRID:AB_2534117) and AF594-conjugated goat anti-rabbit (Thermo Fisher Scientific Cat# A-11037, RRID:AB_2534095), both used at 1:300 dilution. Slices were again washed and mounted on glass slides (Assistant, Karl Hecht ref. 42406020) beneath a 1.5 thickness glass coverslip (VWR 631-0147) in Mowiol. Individual sections of all three animals were stained for either PV or CB1R.

Images were acquired with an ANDOR Dragonfly microscope with 40× water immersion objective (Nikon MRD77410, Apochromat LWD λS 40×, NA 1.15) and pinhole disk with 40 μm hole diameter. Fluorescence stacks of the CA3 subfield were imaged with pixel size of 0.153 μm in xy, with 0.259 μm z-steps. Two individual image planes depicting different cells were taken from each hemisphere of all animals (3 animals × 2 hemispheres × 2 images = 12 images per condition) for analysis. 50 NeuN positive somata per image were segmented manually using ImageJ,[65] blind to other fluorescence channels. Somatic perimeter regions-of-interest were defined as the area 1 μm inside and outside of segmented soma edges, while somatic center regions are defined as the area central to the perimeter ring region. Mean PV and CB1R fluorescence intensity (16-bit pixel values) was measured in perimeter and center regions of all cells. Due to labeling of PV neuronal dendrites and somata by anti-PV antibodies, a subset of segmented cells contaminated with such fluorescence was discarded from further analysis. The distance between the centroid of segmented somata and the *stratum pyramidale-stratum lucidum* boundary was calculated and presented as cell "depth". Mean fluorescence intensity of perimeter and center regions was background subtracted (from fluorescence intensity of "off-slice" regions) and normalized to the mean intensity of all perimeter regions per image, allowing comparison between somata of different depths in images with variable fluorescence intensity values. Somatic center fluorescence in PV and CB1R channels is considered "slice background" levels, and therefore subtraction of this value gives an approximation of relative perisomatic innervation levels (see Figure S5E).

Cell classification

CA3 PN classification into "deep" or "superficial" subclasses was performed using a multi-step procedure. First, cells were provisionally classified morphologically as classical "thorny" PNs, or PNs with athorny cellular morphology (deep somatic location and thin primary dendrite with long distance to first branchpoint (typically over 50 μm), following[23]), either without or with visible thorny excrescences. Next we performed LDA classification from depth/bursting scatterplots of only these morphologically identified neurons with optimal recording conditions (resting membrane potential < −50 mV, no current injection required to maintain V_{mem}, R_{input} in the range 20–500 MΩ). Requirements for "deep" PN classification were then set as follows: somatic depth-burst firing relationship beyond the LDA segregation cut off ([Max burst freq, Hz] = −1.29 × [Somatic depth, μm] + 124.37, as well as passing minimal cutoffs of somatic depth >30 μm, maximum burst frequency >40 Hz, and initial ISI of <0.1 s. All athorny-like neurons (with or without thorns) in the "deep-bursting" cluster by this definition, were classified as "deep" PNs, while all classical thorny neurons outside these criteria were classified as superficial neurons. 16 cells had a mismatch between clustering based classification and provisional morphological classification. These cells were morphologically reassessed and 8 were assigned to their respective LDA-based classification. 2 apparent "superficial athorny" cells, and 3 PNs with deep somatic location but immediate dendritic branching and abundant thorny excrescences, were deemed unclassifiable and were excluded. These criteria were extended to classify 52 neurons which had incomplete morphology but measurable somatic depth and adequate firing properties. Cells without measurable somatic depth or suboptimal recording quality were excluded from further analysis (*n* = 164).

QUANTIFICATION AND STATISTICAL ANALYSIS

All data are reported as mean ± SEM in text and figure legends unless otherwise specified. Boxplots depict data as median (line), 25th and 75th quartile (box) and min/max points (whiskers). Symbols with errors depict mean ± SEM. Connectivities are presented

as bars (measured data) with standard deviation estimated from a binomial distribution. Where individual datapoints are presented overlaid with a line, this line represents the median value unless otherwise stated. Statistical tests are reported in figure legends in all cases. As biological datasets rarely exhibit a normal distribution, non-parametric statistical tests for either two-sample (Mann-Whitney test) or multi-sample (Kruskal-Wallis test) data were applied as appropriate, unless specified otherwise in the figure legend. Where Kruskal-Wallis test has been applied, pairwise comparisons presented on graphs are a result of Dunn's multiple comparison test. Statistical tests were performed using GraphPad Prism 10, and exact p values were reported on figures throughout the manuscript. Proportional datasets (e.g., for connectivity) were compared using Fisher's exact test, either for multisample data (implemented in R), or as individual pairwise comparisons (run using GraphPad Prism) with a Benjamini-Hochberg correction for multiple comparisons.